# Time-Resolved Areal-Density Measurements with Proton Spectroscopy in Spherical Implosions

V. A. Smalyuk, P. B. Radha, J. A. Delettrez, V. Yu. Glebov, V. N. Goncharov, D. D. Meyerhofer,* S. P. Regan, S. Roberts, T. C. Sangster, J. M. Soures, and C. Stoeckl

*Laboratory for Laser Energetics, University of Rochester, 250 East River Road Rochester, New York 14623*

J. A. Frenje, C. K. Li, R. D. Petrasso,† and F. H. Séguin

*Plasma Science and Fusion Center, Massachusetts Institute of Technology, Cambridge, Massachusetts 02139*

(Received 26 September 2002; published 2 April 2003)

The temporal history of the target areal-density near peak compression of direct-drive spherical target implosions has been inferred with 14.7-MeV deuterium-helium-3 $D^3He$ proton spectroscopy of the 60-beam, 30-kJ UV OMEGA laser system. The target areal-density grows by a factor of ~8 during the time of neutron-production ( ~ 400 ps) before reaching $123 \pm 16$ mg/cm$^2$ at peak compression in the implosion of a 950-$\mu$m-diam, 20-$\mu$m-thick plastic CH capsule filled with 4 atm of $D^3He$ fuel.

DOI: 10.1103/PhysRevLett.90.135002 PACS numbers: 52.35.Py, 52.50.Jm, 52.70.La

The goal of inertial confinement fusion (ICF) [1,2] implosions is to achieve sufficiently high temperature and compression within deuterium-tritium (DT) fuel to sustain a thermonuclear burn. The burn begins with spark ignition of the central hot spot [2] that is created as a result of shock heating while the target compresses. A burn wave then propagates into the higher-density regions of the compressed fuel-shell, releasing energy through thermonuclear reactions [2]. The combination of high temperature in the hot spot and high density-radius product (areal-density or $\rho R$) in the compression fuel is necessary to ignite the target and achieve high gain [1–3]. Areal densities measured so far in cryogenic implosions [4–7] are far below values necessary for ignition both because low laser energy (25 kJ or less) is available and the unstable growth of target and laser-induced perturbations limits the compression. In recent implosions on the 60-beam, 351-nm OMEGA laser system [8], average areal densities of ~80 mg/cm$^2$ have been achieved with cryogenic $D_2$ targets and laser energies of ~17–23 kJ [7].

Measurements of compression dynamics and uniformity are fundamental for quantifying the implosion performance and vital in determining factors compromising its outcome. Areal-density evolution measurements in cryogenic $D_2$ or DT implosions are complicated by lack of simple and reliable diagnostic techniques that are available with plastic shells. Therefore many experimental studies in ICF are performed with "cryo surrogates," hydrodynamic-equivalent plastic shells. As an example, this Letter describes implosions of plastic shells filled with $D^3He$ gas fuel. The primary fusion reactions in $D^3He$ fuel are $D + D \rightarrow {}^3He(0.82\ \mathrm{MeV}) + n(2.45\ \mathrm{MeV})$ and $D + {}^3He \rightarrow {}^4He(3.6\,\mathrm{MeV}) + p(14.7\,\mathrm{MeV})$. Measured neutron-production history (DD fusion) is combined with the primary 14.7-MeV proton spectra ($D^3He$ fusion) to infer, for the first time, the areal-density growth during the period of neutron-production.

Until recently, all reported values of target compression have been time averaged over the interval of neutron and charged-particle production [9–11]. Time-integrated proton spectra (used to measure average $\rho R$) clearly show signatures of time-dependent $\rho R$ evolution. Primary proton spectra from implosions of 24-$\mu$m-thick shells show two distinctive features from the shock and compression phases of implosion [12]. These features can be produced only if the total $\rho R$ differs by a factor of ~10. Time-integrated, 14.7-MeV proton spectra are formed by the protons emitted during period of proton production in $D^3He$ fusion reaction. During this time the capsule $\rho R$ grows as the target compresses. Protons emitted from the $D^3He$ fuel lose energy when passing through the capsule (mostly in the plastic shell material). The amount of energy loss is determined by the areal density of target material through which the protons pass. Therefore, it is possible to infer target $\rho R$ temporal evaporation from the measured time-integrated proton spectra, provided that the proton-production history is known (or can be estimated) and the $\rho R$ increases nearly monotonically during particle-production. Other factors contributing to the shape of the measured proton spectrum include geometrical broadening, ion temperature, small-scale shell mass modulations, and the detector spectral response. The geometrical broadening of the proton energy spectrum is due to the finite size of the proton-production region. Even in a uniform spherical target (without modulations) protons pass through the compressed shell at different angles, sampling a range of path lengths through the shell. Since the proton energy loss is proportional to the path length through the shell, the energy spectrum of protons emitted from the target is broader than the original spectrum. Similarly, small-scale, shell

  

areal-density mass modulations also broaden the proton spectra by introducing a range of path lengths for protons.

The areal-density evolution is inferred by fitting a constructed proton spectrum $P_c(E)$ to the measured $P_m(E)$ proton spectrum. The assumptions made during fitting are the following: (1) The proton stopping power is independent of target density and temperature; (2) The dimensions of the proton production and whole fuel regions (used in geometrical broadening calculations) and the ion temperature are constant in time at their neutron-averaged values; (3) The $D^3He$ proton-production history is proportional to the DD neutron-production history (this assumption is consistent with that of a constant ion temperature). As discussed below, one-dimensional (1D) hydrodynamic simulations support all of these basic assumptions. The spectrum $P_c(E)$ is constructed using the measured DD neutron-production rate and the target areal density $\rho R_t(t)$ assumed to have a Lorentzian form as a function of time $t$, $\rho R_t(t) = C_0/[(t - C_1)^2 + (C_2/2)^2]$, consistent with the 1D simultaneous. In the fitting procedure, at any time $t$ the initial proton energy is 14.7 MeV and the proton-production rate is assumed to be proportional to the DD neutron-production history. At this time, the proton spectrum undergoes ion temperature and the geometrical broadening, is downshifted by the target areal density of $\rho R_t(t)$, and then broadened by the detector spectral response. The proton spectrum $P_c(E)$ is constructed by summing the protons at energy $E$ for all times. The best fit is achieved using a $\chi^2$ minimization of the deviation between $P_c(E)$ and $P_m(E)$ by varying the three fitting parameters $C_0$, $C_1$, and $C_2$. The above approximations result in small uncertainties included in the error bars of the inferred $\rho R$ evolutions. The fitting procedure and assumptions made have been tested using the simulations of the 1D hydrocode LILAC [13].

The geometric broadening of the proton spectrum is described schematically in Fig. 1. To estimate the broadening, it is assumed the gas fuel and proton-production region have radii $R_2$ and $R_1$, respectively, and the compressed radius of the target is $R_3$. On the way to a distant detector (assuming parallel trajectories), protons lose their energy primarily in the shell of thickness $R_3$-$R_2$. Protons that are emitted along the $x$ axis pass through the minimum thickness of the shell material, while protons that are emitted parallel to but off this axis have a longer path length. As a result, even for a uniform shell, the protons reaching the detector will have an energy spread since the proton energy loss depends on the path length through the shell. Figure 1(b) shows calculated spectra of monoenergetic 14.7-MeV protons after passing a uniform shell of various areal densities for target parameters $R_1 = 27$ $\mu$m, $R_2 = 33$ $\mu$m, and $R_3 = 63$ $\mu$m given by LILAC. The number of protons reaching the detector in the $x$ direction as a function of the orthogonal coordinate $z$ ($0 \le z \le R_1$) have a distribution $F(z) = Cz\sqrt{R_1^2 - z^2}$,

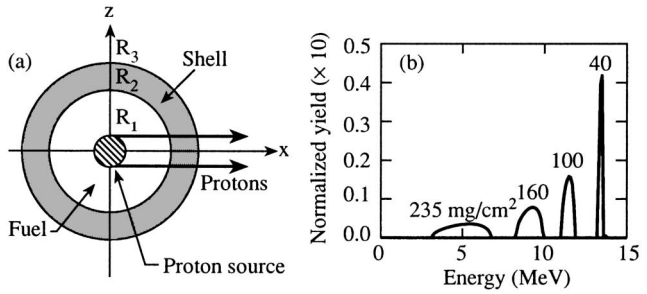


FIG. 1. The geometrical broadening effect. (a) Target schematic: The proton-production region has a radius of $R_1$, the gas has a radius of $R_2$, and the shell has a thickness of $R_3$-$R_2$. Protons travel to a distant detector in the direction of and parallel to the $x$ axis; (b) the geometrically broadened shapes, as normalized 14.7-MeV proton spectra, after passing through target areal densities of 40, 100, 160, and 235 mg/cm$^2$, $R_2 = 33$ $\mu$m.

where $C$ is a constant derived using the target geometry shown in Fig. 1(a). The effective areal density seen by the detected protons is $\rho R_{\text{eff}}(z) = \rho[\sqrt{R_3^2 - z^2} - \sqrt{R_2^2 - z^2}]$. Substituting $z$ for $\rho R_{\text{eff}}$ in the expression for $F(z)$ and converting $\rho R$ to proton energy using the curve described later in Fig. 2(c) results in the geometrically broadened shapes shown in Fig. 1(b). The original monoenergetic proton spectrum broadens and shifts to lower energies.

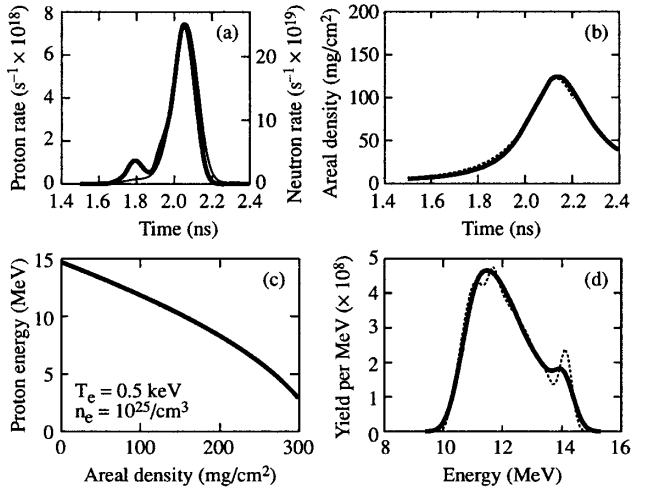


FIG. 2. (a) LILAC simulations of proton (thick line) and scaled-neutron (thin line) production histories. The two peaks correspond to first production at shock coalescence and subsequently during the compression phase. During the compression phase, the neutron and proton production rates have the same temporal history; (b) target areal-density evolution from a LILAC simulation (solid line), and from fitting (dotted line); (c) theoretical proton energy versus target areal density calculated using Bethe-Bloch stopping power for an electron density of $10^{25}$ cm$^{-3}$ and a temperature of 0.5 keV; (d) time-integrated proton energy spectra from LILAC simulation (solid line) and from fitting (dotted line).

Figure 2 shows the results of a simulation of shot 21240 with 15 atm $D^3He$ fill, performed with LILAC; these results were used to develop and test a fitting procedure to determine the area-density evolution. Figure 2(a) shows $D^3He$ proton-production history (thick solid line) used in this fitting (the neutron-production history is shown by the thin line for comparison). Note that the proton and neutron-production rates are calculated to be essentially identical during the compression phase, due to the relative constancy of the ion temperature, validating the use of the neutron-production rate as an estimate of the proton-production rate. The different ion-temperature-dependent cross sections for the DD and $D^3He$ fusion reactions could lead to small differences in the proton- and neutron-production rates [see Fig. 2(a)] if the ion temperature changes during implosion. For example, there is a discrepancy in the shock yield at $\sim$1.8 ns. In the experiment, the measured shock yield is much smaller than suggested by the simulation shown in Fig. 2(a). This is because the measured ion temperature ( $\sim$ 5.5 keV) during the shock is smaller [12] than that predicted by the simulation ( $\sim$ 8 keV).

At any particular time $t$, the protons (their flux is given by the production history) have their initial energies (14.7 MeV) broadened by the neutron-averages ion temperature of $\sim$3.4 keV (assumed to be constant throughout the production). The spectrum of these protons leaving the target [with the areal density $\rho R_t$ $(t)$ set by three fitting parameters $C_0$, $C_1$, and $C_2$] is additionally broadened by the geometrical effect and downshifted according to Fig. 1(b). Finally, the constructed spectrum $P_c(E)$, which is the sum of all proton spectra generated during proton production, is broadened by the instrumental spectral response ( $\sim$ 0.2 MeV). The target $\rho R$ evolution [Fig. 2(b), dotted line] is inferred from the best fit during $\chi^2$ minimization of the deviation between $P_c(E)$ and $P_m(E)$ [Fig. 2(d), dotted and solid lines, respectively] by varying the fitting parameters $C_0$, $C_1$, and $C_2$. Good agreement between the predictions of areal density from the fitting procedure [Fig. 2(b), dotted line] and the LILAC simulations (solid line) shows that all approximations are reasonable and the uncertainties associated with them are small. The Bethe-Bloch stopping power [14] was used in the fitting procedure; it depends weakly on the plasma density and temperature. The theoretical slowing-down curve shown in Fig. 2(c) has been calculated for a fully ionized CH plasma with an electron density of $10^{25}$ $cm^{-3}$ (corresponding to plastic density of $\sim$35 $g/cm^3$) and an electron temperature of 0.5 keV.

Direct-drive implosions were carried out on the 60-beam OMEGA laser system. The targets were $\sim$950-$\mu$m-diam, 20-$\mu$m-thick plastic shells filled with 18 or 4 atm of $D^3He$ gas. Targets with 4 and 18 atm of $D^3He$ gas exhibit similar behavior during their laser-driven acceleration phases and therefore have similar perturbations at the beginning of the deceleration phase. Because of their differing gas-fill pressures (4 and 18 atm), these targets experience different deceleration-phase growth near peak compression. Targets with 4-atm fill have a longer deceleration phase and are therefore more unstable. The targets were imploded with a 1-ns square pulse shape with a total on-target energy of $\sim$23 kJ. All laser beams were smoothed with distributed phase plates [15], 1-THz, two-dimensional smoothing by spectral dispersion [16], and polarization smoothing [17] using birefringent wedges. The average beam-to-beam energy imbalance was 3–4%. The neutron-production histories from the DD reaction were measured with the neutron temporal diagnostic (NTD) [18]. Proton spectra from the $D^3He$ reaction were measured with seven wedge-range filters (WRF's) [19] to sample different views of the target. Combining data from implosion experiments with an equivalent mass of $D_2$ and DT fuel, values of neutron yield and ion temperature (from scintillators), neutron burn history (NTD)] [18], and average fuel areal density (knock-on deuterons) [11], are used to estimate the radii of the particle-production ($R_1$) and fuel regions ($R_2$) at peak neutron-production. These are required to estimate the extent of geometrical and thermal broadening contributions to the shapes of proton spectra. For example, from implosions with 15-atm-DT fuel (mass equivalent to 18 atm of $D^3He$), $R_2 = 36$ $\mu$m has been calculated using conservation of fuel mass ($8.3 \times 10^{-7}$ g) and measured fuel $\rho R$ ( $\sim$ 15 $mg/cm^2$) [11]. In order to match the experimental neutron yield of $\sim 1.6 \times 10^{11}$, the particle-production volume requires $R_1 =$ 22 $\mu$m at the measured neutron-averaged ion temperature of $\sim$3.7 keV and neutron burn width of $\sim$170 ps. The shell thickness $R_3$-$R_2$ (the least sensitive parameter in the proton spectral fits) has been taken to be 30 $\mu$m based on estimates from x-ray images.

Figures 3(a) and 3(b) show proton spectrum fitting results for shot 25220 with 18 atm of $D^3He$ gas for two (out of seven) representative detectors (the jagged lines correspond to experimental data and the smooth lines to fitting results). The inferred total areal-density time histories for all seven directions are shown by solid lines in Fig. 3(c) together with the measured neutron-production history (dashed line) from the same shot. Protons reaching the WRF detectors probe the shell area with a diameter of about 50 $\mu$m (corresponding to a mode number $\ell = 6$). Seven WRF detectors, approximately uniformly distributed around the spherical target, are sensitive to low-mode asymmetries with mode numbers $\ell < 6$. Small-scale, shell $\rho R$ modulations with mode numbers $\ell > 6$ broaden and additionally downshift the proton spectra in each WRF detector view by increasing, relative to a uniform shell, the range of path lengths for proton energy loss. The inferred $\rho R$ modulation level of about 7% at peak neutron-production and its growth by a factor of 2 up to peak compression, as calculated by 2D simulations [20], was used to account for this broadening and energy downshift. Thus, $\sim$70% of the total width of a time-integrated proton spectrum is estimated to be due to

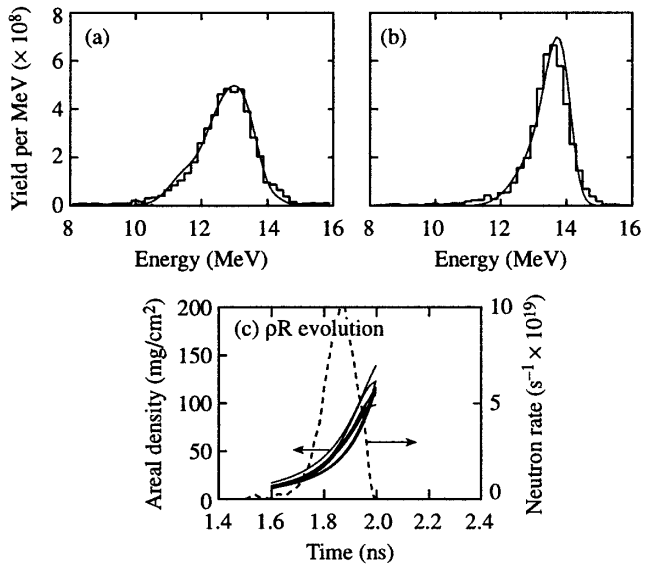


FIG. 3. (a),(b) The proton spectra and fitted results (smooth solid lines) for shot 25220 in two directions with 18 atm of $D^3He$ gas. (c) Inferred areal-density evolution from seven directions (solid lines) and the neutron-production history (dotted line) for this shot.

areal-density evolution, ~20% due to geometrical effects, and the remaining ~10% is due to temperature, short-scale length (with mode numbers $\ell > 6$) areal-density perturbations, and instrumental broadening.

Figure 4 summarizes the inferred areal-density evolution for implosions with 18-atm [Fig. 4(a)] and 4-atm $D^3He$ fills [Fig. 4(b)] and curves of 1D LILAC predictions. The more-stable 18-atm-fill shot has an inferred peak $\rho R$ of $109 \pm 14$ mg/cm$^2$ (thick solid line), which is close to the 1D prediction (thin solid line); however, the more-unstable 4-atm shot has an inferred peak areal density of $123 \pm 16$ mg/cm$^2$, much lower than the theoretical prediction of 230 mg/cm$^2$. The higher fuel-shell mix (due to modulation growth) in the more-unstable 4-atm implosion is responsible for increased core pressure that prevents target compression to 1D values [10,21]. During the period of neutron-production (from 1.6 to 2.0 ns), the $\rho R$ grows by a factor of ~8 in the 4-atm shot. The observed areal-density growth throughout particle emission confirms indications from earlier spectroscopic results [21]. At peak compression, the areal-density asymmetries with low-mode numbers $\ell < 6$ are ~10% and ~20% for 18-atm and 4-atm-fill targets, respectively, as estimated from the measured values in seven detectors. The measured peak areal density is only about 10% higher for the 4-atm-fill target than the 18-atm-fill target due to unstable modulation growth and fuel-shell mixing.

In conclusion, the target areal density grows by a factor of ~8 during the time of neutron-production ( ~ 400 ps) before reaching $123 + 16$ mg/cm$^2$ at peak compression in the shot with a 20-$\mu$m-thick plastic CH target filled with 4 atm of $D^3He$ fuel. This value is lower, by a factor of 2,

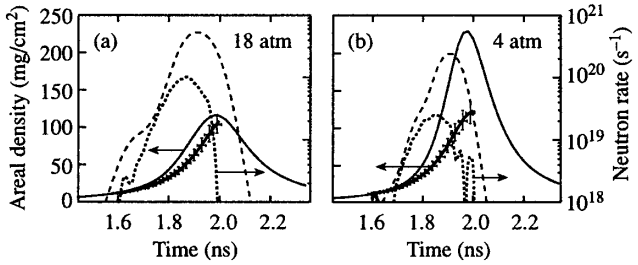


FIG. 4. The measured (thick solid line) and simulated (thin solid line) target areal-density evolutions for (a) 18-atm and (b) 4-atm implosions. Measured (dotted line) and simulated (dashed line) neutron-production histories for (a) 18-atm and (b) 4-atm shots.

than the 1D prediction of 230 mg/cm$^2$, as a result of unstable modulation growth leading to fuel-shell mix. For the more-stable, 18-atm-fill target, the target areal density reaches $109 \pm 14$ mg/cm$^2$ at peak compression, much closer to the 1D prediction of 115 mg/cm$^2$. The experiments suggest that improved beam-to-beam power and energy balance and/or more-stable designs are necessary to mitigate the detrimental effect of fuel-shell mix on target compression.

This work was supported by the U.S. Department of Energy Office of Inertial Confinement Fusion under Cooperative Agreement No. DE-FC03-92SF19460, the University of Rochester, and the New York State Energy Research and Development Authority.

*Also Departments of Mechanical Engineering, and Physics and Astronomy.
†Visiting Senior Scientist, Laboratory for Laser Energetics.

[1] J. H. Nuckolls *et al.*, Nature (London) **239**, 139 (1972).
[2] J. D. Lindl, Phys. Plasmas **2**, 3933 (1995).
[3] P.W. McKenty *et al.*,Phys. Plasmas **8**, 2315 (2001).
[4] R. R. Johnson *et al.*, Phys. Rev. A **41**, 1058 (1990).
[5] F. J. Marshall *et al.*, Phys. Rev. A **40**, 2547 (1989).
[6] K. A. Tanaka *et al.*, Phys. Plasmas **2**, 2495 (1995).
[7] T. C. Sangster *et al.* [Phys. Plasmas (to be published)].
[8] T. R. Boehly *et al.*, Opt. Commun. **133**, 495 (1997).
[9] M. D. Cable *et al.*, Phys. Rev. Lett. **73**, 2316 (1994).
[10] C. K. Li *et al.*, Phys. Rev. Lett. **89**, 165002 (2002).
[11] C. K. Li *et al.*, Phys. Plasmas **7**, 2578 (2000).
[12] R. D. Petrasso *et al.*, Phys. Rev. Lett. **90**, 095002 (2003).
[13] J. Delettrez *et al.*, Phys. Rev. A **36**, 3926 (1987).
[14] T. A. Mehlhorn, J. Appl. Phys. **52**, 6522 (1981).
[15] Y. Lin, T. J. Kessler, and G. N. Lawrence, Opt. Lett. **20**, 764 (1995).
[16] S. P. Regan *et al.*, J. Opt. Soc. Am. B **17**, 1483 (2000).
[17] T. R. Boehly *et al.*, Opt. Commun. **133**, 495 (1997).
[18] R. A. Lerche *et al.*, Rev. Sci. Instrum. **66**, 933 (1995).
[19] F. H. Séguin *et al.*, Phys. Plasmas **9**, 2725 (2002).
[20] V. A. Smalyuk *et al.*, Phys. Plasmas **9**, 2738 (2002).
[21] S. P. Regan *et al.*, Phys. Rev. Lett. **89**, 085003 (2002).